Improved Rate Capability for Dry Thick Electrodes Through Finite Elements Method and Machine-Learning Coupling

Mehdi Chouchane[1], Weiliang Yao[2], Ashley Cronk[2], Minghao Zhang[3,],*

*and Ying Shirley Meng[1, 3]***

[1] Pritzker School of Molecular Engineering, University of Chicago, Chicago, IL, USA

[2] Materials Science and Engineering, University of California San Diego, La Jolla, CA, USA

[3] Department of NanoEngineering, University of California San Diego, La Jolla, CA, USA

Corresponding Author

* miz016@eng.ucsd.edu

** shirleymeng@uchicago.edu

A coupled Finite Elements Method (FEM) and Machine-Learning (ML) workflow is presented to optimize the rate capability of thick positive electrodes (ca. 150 µm and 8 mAh/cm²). An ML model is trained based on the geometrical observables of individual LiNi0.8Mn0.1Co0.1O2 particles and their average state of discharge (SOD) predicted from FEM modeling. This model not only bypasses lengthy FEM simulations, but also provides deeper insights on the importance of pore tortuosity and the active particles size, identified as the limiting phenomenon during the discharge. Based on these findings, a bi-layer configuration is proposed to tackle the identified limiting factors for the rate capability. The benefits of this structured electrode are validated through FEM by comparing its performance to a pristine mono-layer electrode. Finally, experimental validation using dry processing demonstrates a 40% higher volumetric capacity of the bi-layer electrode when compared to the previously reported thick NMC electrodes.

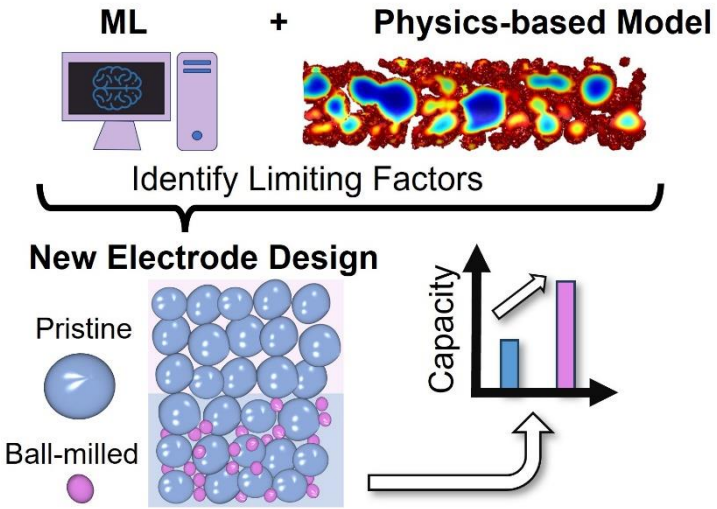

A promising route to reach higher energy densities is increasing the thickness of the electrodes to maximize the loading of active materials. By increasing the active material volume within the electrode, larger amounts of energy can be stored, enabling electric vehicles (EVs) to travel longer distances on a single charge. However thick electrodes are widely recognized for their inadequate rate capability,[1] leading to an even lengthier charging time for EVs compared to the already lengthy current duration. The main bottleneck hindering fast (dis)charging is still being debated in the scientific community.[2] Putting aside the mechanical challenges,[3,4] it can be attributed either to the limited electronic conductivity due to a tortuous carbon network, or the poor wettability caused by a tortuous pore phase which will lead to a sluggish ionic transport.[5,6]

Modeling can serve as a valuable tool for guiding experimental design and identifying limiting factors within a system.[7,8] 3-D digital twins have been used in the context of thick electrodes first by Danner *et al.* to highlight the importance of the connectivity of the electronically conductive network throughout all the thickness of the electrode.[8] Lu *et al.* quantified the heterogeneity within an electrode in terms of state of lithiation based on its thickness.[9] However, the use of computationally expensive 3-D Finite Elements Method (FEM) simulations restricts the ability to thoroughly analyze a wide range of parameters and their individual impacts. Machine-Learning (ML) is a suitable approach to accelerate the predictions, even for experimental inputs with for instance Severson *et al.*[10] who could accurately predict the cycle life (nominal capacity > 80%) of a cell based on the first 100 cycles. Recently, Marcato *et al.*[11] employed ML coupled with FEM simulations to predict the spatial distribution of the state of discharge (SOD) in 3-D and discharge curves. Although this approach significantly reduces the time and resources required for accurate predictions, it still lacks deeper insights regarding the relationship between the SOD and the

electrode's features. In the context of thick electrodes, only the graphite electrodes have been studied, either through the optimization of the pore-channel design[12,13] or the prediction of the performance based on the manufacturing parameters.[14]

In this work, an ML model is trained using a dataset of FEM simulations to predict the average state of lithiation at different depths of discharge for each $LiNi_{0.8}Mn_{0.1}Co_{0.1}O_2$ (NMC_{811}) particle. The novelty in this approach is to consider each particle in the electrode as a data point instead of each simulation, which will considerably speed up the obtention of a large enough representative dataset (**Scheme 1**). Moreover, through the implementation of Shapley Additive Explanation (SHAP) Values,[15] the contribution of each parameter to the SOD is elucidated, thereby revealing the most prominent hindering phenomena. Based on these findings, a structured bi-layer positive electrode design is proposed to enhance the rate capability. This design is firstly validated via an FEM simulation and subsequently verified experimentally, where the half-cells at a current densities of 8 and 4 mA/cm² (1C and C/2 respectively) demonstrate a volumetric capacity surpassing that of any previously reported NMC thick electrodes at those discharge rates. The electrodes were manufactured using dry coating, which has been highlighted as an effective processing method to obtain mechanically robust and homogeneous thick electrodes.[16]

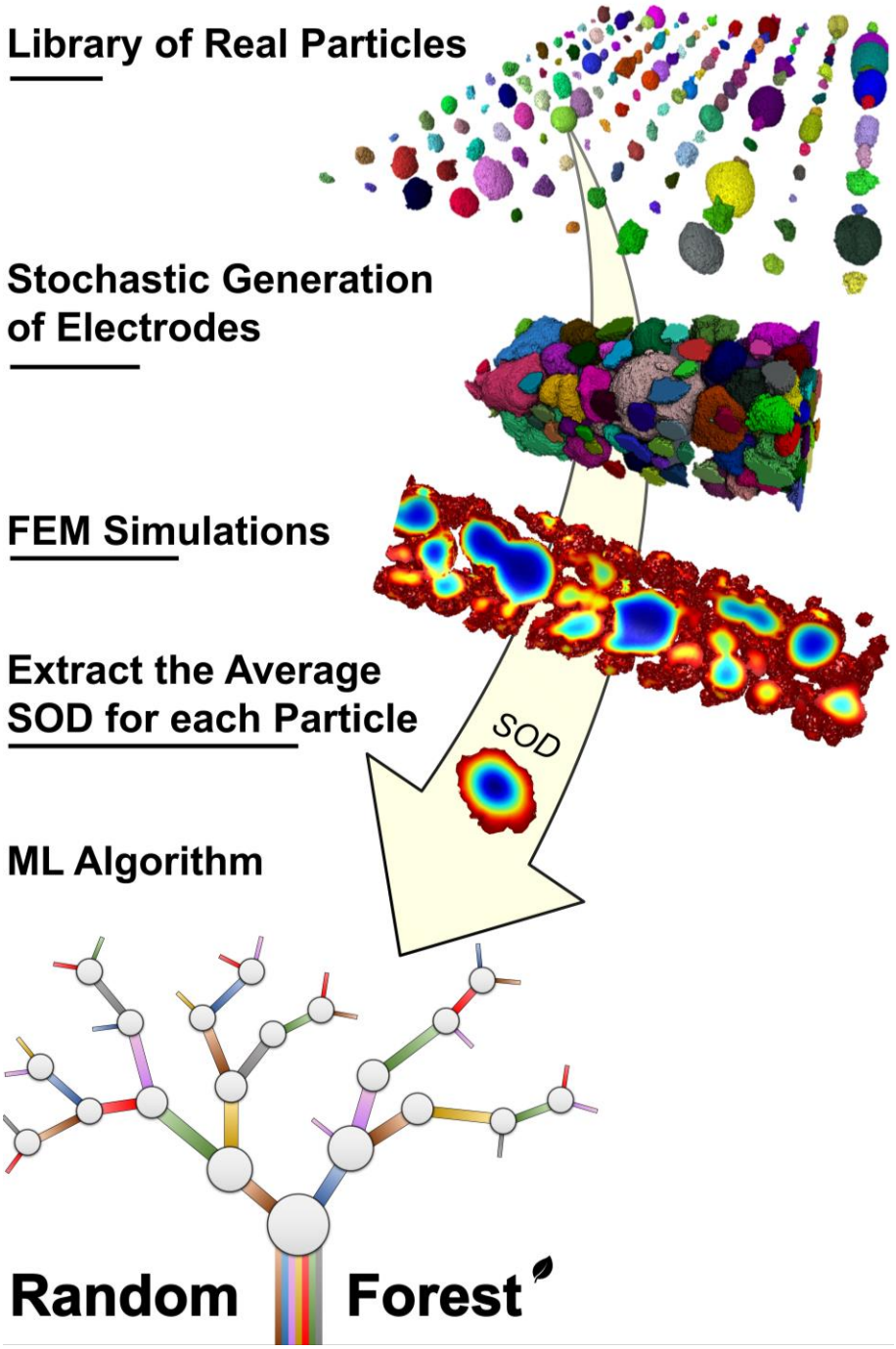

Scheme 1. Workflow of the computational approach developed in this work, from the stochastic generation of electrodes, the finite elements method (FEM) to the training of the machine-learning (ML) model based on the state of discharge (SOD) of each particles. For each step, the scale bar under the label represents 50 µm.

Machine-Learning Validation for Thick Electrode

The system modeled in this work is a 30×30×150 μm^3 electrode with 93 wt% of NMC_{811}, 5 wt% of Vapor Grown Carbon Fibers (VGCF), and 2 wt% of Poly(tetrafluoroethylene) binder (PTFE). For computational strain reasons, the VGCF and PTFE were merged into one single phase known as the Carbon Binder Domain (CBD) in the modeling field.[17] The electrodes were stochastically generated using an in-house MATLAB code, which is provided as well as all the codes and the FEM template used to obtain the results presented in this article. This stochastic algorithm uses real NMC_{811} particles extracted from plasma focused ion beam (PFIB) data,[18] and generates CBD as fibers to mimic the morphology of VGCF and PTFE. The 3-D electrodes were then converted into a mesh using the open access Iso2Mesh toolbox.[19]

The simulations consist of a single discharge at 8 mA/cm^2 (1 C) starting from a completely delithiated electrode, with a cut-off voltage of 3.0 V. A 3-D Newman model extensively used in the literature[20,21] was employed and implemented into COMSOL Multiphysics 5.6[22] to solve the partial differential equations (see Table S1,S2).

The limiting factor to the training of an effective ML model is usually the obtention of a large enough amount of data. Here, only 10 FEM simulations were needed to build a satisfactory training dataset. This was made possible since the ML model will predict an output for individual particles, then in each FEM simulation, each NMC_{811} particle is a datapoint. The ability to characterize individually particles has been introduced fairly recently in the battery modeling field and has pushed forward our capability to provide insights currently impossible to obtain experimentally.[7,9] With an average of 200 particles per electrode (excluding the ones on the borders), 2076 datapoints were extracted at 4 different depths of discharge (DoD), namely 25%, 50%, 75% and 100% in

order to have time-dependent predictions, yielding a total of 8304 datapoints. To increase the understanding of the underlying limiting phenomena and go beyond the work of Marcato et al.,[11] the observables fed to the ML algorithm are geometrical features of the particles/electrodes. Namely, the volume of the NMC particle, its active surface area (surface in contact with the electrolyte), its position along the thickness of the electrode, the surface area in contact with CBD, and the tortuosity of the electrolyte from the separator plane to the particle plane (using TauFactor)[23]. The output of the ML algorithm is the prediction of the average SOD for individual particles at different DoDs.

A random forest algorithm was trained with the as described dataset, and its predictions for a new dataset was compared to the actual FEM simulation outputs in **Figure 1A**. In **Figure 1A**, each point represents a particle at a given DoD, and in an ideal case, all the predictions would be identical to the FEM outputs, hence all the points would be aligned on the x = y black curve. The greater is the distance between this curve and a point, the greater is the prediction error. Here, we can observe a satisfactory agreement between the actual values and the predictions, with an average error of 0.042 (average relative error of 7.3%), thus validating the accuracy of our trained model. An example of an electrode is provided in **Figure 1(B,C)** with the SOD at the end of discharge plotted in 3-D from a FEM simulation and the predictions from the ML algorithm. For both, a uniform intra-particle gradient of concentration was assumed for plotting while keeping the proper average SOD predicted by both modeling methods. Only few particles display a noticeable difference between the FEM simulation and the ML predictions. This is particularly impressive since each COMSOL simulation performed in this work required several hours to compute, while the prediction time for the ML workflow is 2 orders of magnitude lower (around 1 min).

The novelty of this workflow lies in the simplicity to set it up, requiring only 10 FEM simulations and a basic random forest algorithm to achieve such a high accuracy. Moreover, the use of geometrical observables of particles allows to get a deeper understanding of their contribution to the NMC utilization. This work paves the way towards a wider use of ML tools by proposing a quick workflow and by providing all the codes and the COMSOL template necessary.

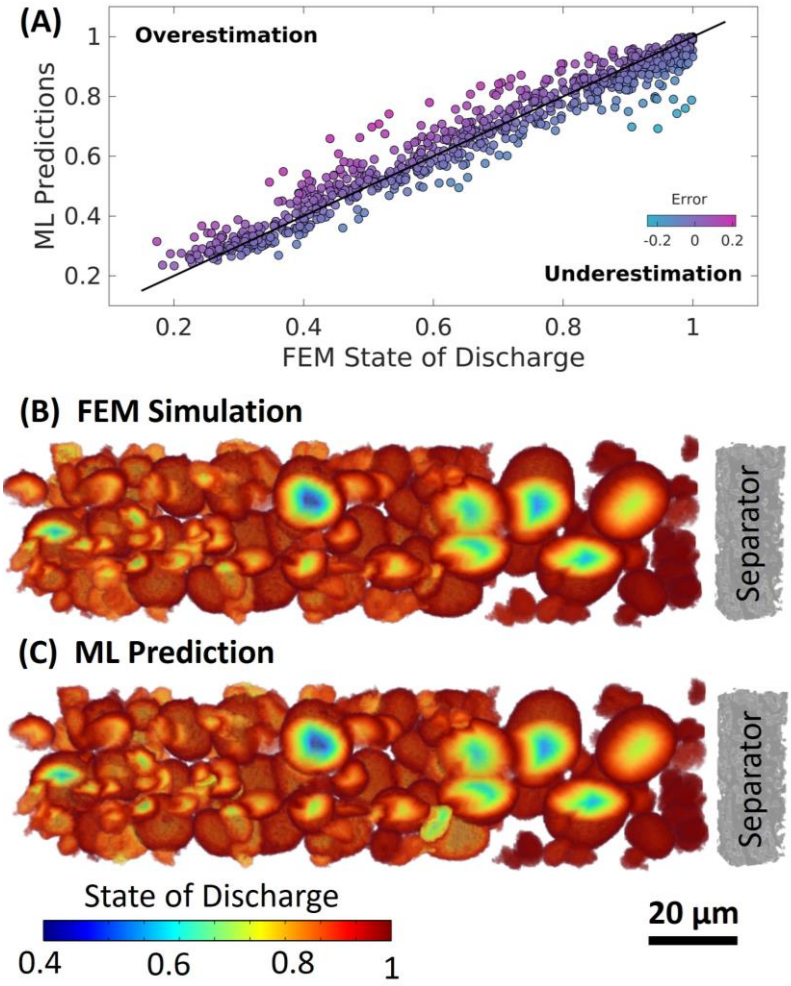

Figure 1. (A) Scatter plot of the ML-predicted values of the state of discharge of individual particles as a function of the values obtained through FEM simulations. The solid black line represents the region where the predictions are identical to the obtained values. 3-D distribution of the state of discharge at the cut-off voltage (3 V) for (B) the FEM simulation and (C) the trained

ML algorithm. The relative gradients representing state of discharge inside individual particles was assumed to be constant and equal to the average value of the relative gradients extracted from FEM simulations.

Limiting Factors for High-Rate Capability

ML algorithms usually suffer from the "black box" syndrome, where their predictions are accurate, but the users cannot unravel further insights on how each input parameters will impact the output. Recently, there has been development in the artificial intelligence field on the topic of explanatory artificial intelligence (XAI).[24] XAI aims to address this issue by providing techniques to have a better grasp at the thought process behind the ML predictions. Among these techniques, the study of the Shapley additives explanation (SHAP) values has been on the rise in the battery field.[25,26] The strength of this approach is to identify for each input feature its impact on the SOD depending on its relative value, for instance the impact of large or a small value of CBD contact would have on the predicted SOD. In essence, sub-ML algorithms of all the combinations with a lower amount of input features will be trained. For each data point, the evolution of the prediction when introducing a new input feature in the ML model will be studied. For instance, let us consider a data point consisting of an NMC_{811} particle with a given volume and active surface area. Starting from an ML model with the only input being the volume of the particle, a first prediction of the SOD would be obtained. Then, a second model would be trained with both features, and its SOD prediction for this given particle would be compared to the prediction of the 1-feature model. If by introducing the active surface area of the particle in the model, the predicted SOD would increase, then the SHAP value for this data point and the active surface area feature would be positive,

because it had a positive impact on the predicted SOD. If the predicted SOD is lower after adding the active surface area as a second input, then the SHAP value would be negative. The weakness of this method is the computational cost necessary to train all the sub-ML algorithms which hinders its practical use. However, Lundberg et al. were successful in reducing the complexity of SHAP calculations for tree-based models, [27,28] thus allowing us to compute their values for each feature in the ML algorithm.

Figure 2A displays the SHAP values for all the data point of the validation dataset, and each feature is ranked from the most to the least impactful from top to bottom. The ionic transport through the electrolyte tortuosity is the feature with the highest range of SHAP values, with low tortuosity inducing a better NMC_{811} utilization. Indeed, from **Figure 2B** the electrolyte tortuosity as well as the average SOD are plotted as a function of the distance from the current collector from ML predictions. Opposite trends can be observed, with the NMC_{811} particles being more utilized near the separator, while the tortuosity increases as we get closer to the current collector. It corroborates the impact of the tortuosity of the electrolyte on the particles' utilization as highlighted by **Figure 2A**. Regarding the volume of the NMC_{811} particles, it transpires that smaller particles will have a higher SOD than larger particles, which is in agreement with the current studies in the literature to optimize the particle size of active material.[29] Further investigations on the distribution of the SOD for NMC_{811} particles separated into 3 groups (**Figure 2C**) demonstrates that the peak of distribution for larger particles corresponds to a lower SOD than the other groups. Interestingly, the "Small particles" group has a wider distribution of SOD than the others, which can be explained by the difficulty to connect all the smaller particles to the carbon network. Indeed, **Figure S1** sheds light on the lower current density at the surface of the "Small Particles" compared to the larger NMC_{811} particles.

The third most impactful feature is the thickness position of the particle (0 µm being the current collector), with particles closer to the separator experiencing a higher lithiation than the particles close to the current collector. This phenomenon can also be attributed to systems limited by the ionic transport, as mentioned in the literature.[7,9] Lastly, the active material surface and the contact with the carbon network are both following the same trend, the higher the feature value the higher the SOD. Here, the contact with the CBD phase has a minor impact on the SOD because the fiber morphology and the homogeneous distribution of the VGCF enables an efficient electronic network for all the NMC_{811} particles.

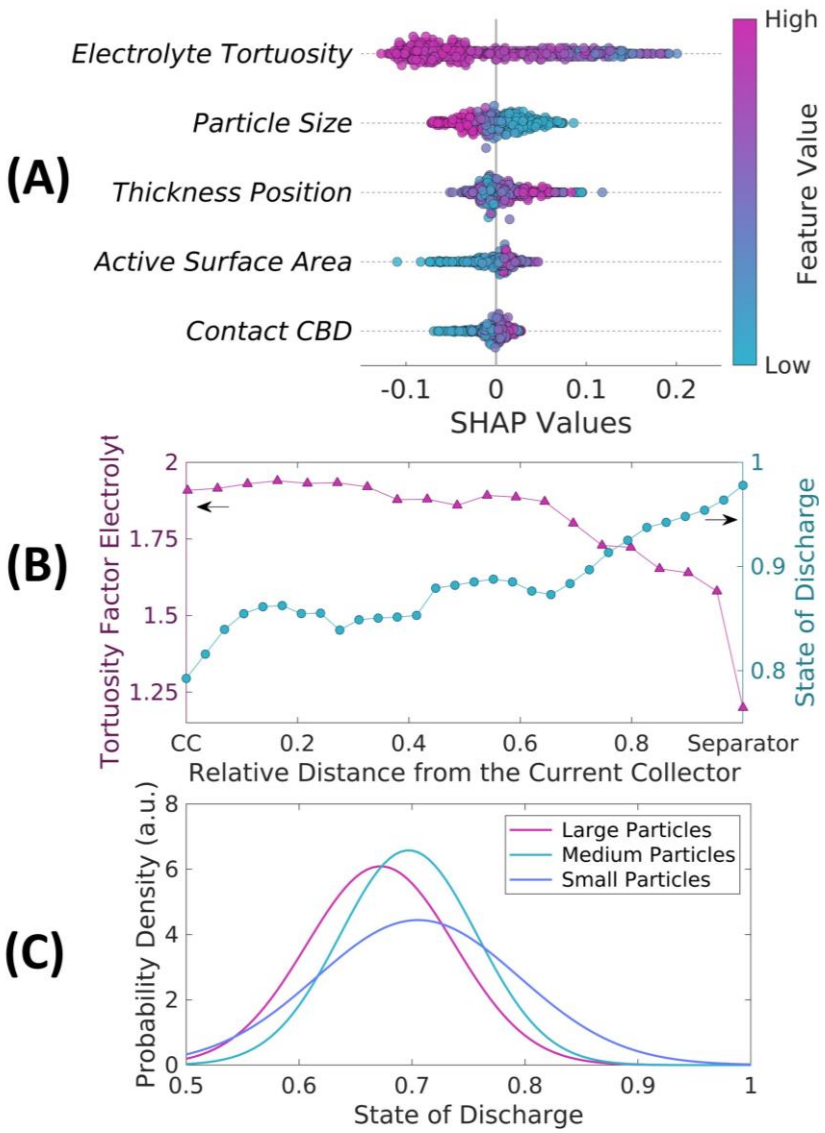

Figure 2. (A) Plot of the SHAP values extracted from the trained ML algorithm for the different features. Each point represents a data point of the dataset used for verification, and the color code is a function of the relative value of each parameter. (B) The tortuosity factor in the electrolyte and CBD measured from the separator to different depths of the electrode and the average state of discharge (from ML) as a function of the distance from the current collector. (C) Fitted normal distributions of the state of discharge of the NMC_{811} particles of the half of the electrode closer to the current collector (where differences are higher) divided into three groups based on the volume of NMC particles.

Structured Bi-layer Electrode

Due to the coupled FEM-ML workflow, the most impactful features have been identified in the context of fast discharge for thick NMC_{811} electrodes, with the tortuosity of the pores network at the top of the list. While there has been many research on how to decrease tortuosity in thick electrodes using laser structuring,[30] its use can lead to a deterioration of the mechanical integrity of the electrode,[31] and its scalability and practical use at an industrial scale are still under development,[32] Therefore, this work will focus on the second most impactful feature to improve the electrochemical performance, namely the volume of the NMC_{811} particles. As evidenced by **Figure 3A**, smaller particles tend to have a higher SOD than larger particles. Reducing the size of the particle will in turn increase the specific active surface area which is beneficial to the NMC_{811} utilization according to the SHAP values. Also, in **Figure 3B** we observe a poor utilization of the NMC_{811} in the lower half of the electrode, i.e. the half closer to the current collector. These observations motivated the suggested bi-layer design, where the top layer, i.e. the one close to the separator, will remain unchanged, but the bottom half will consist of a mix of pristine (75 wt.%) and ball-milled (25 wt.%) NMC_{811} particles. This ratio was chosen based on the quickly degrading mechanical properties of the film with higher ball-milled particles content. Also, using the dry process, the layer with a mix of NMC_{811} would achieve a higher degree of compaction during the rolling step with a higher number of ball-milled particles, increasing the tortuosity of the pore network and hindering its performance. The added ball-milled particles with a lower volume and higher specific active surface area should help in achieving a higher utilization. Also, one might expect to have the mixed NMC_{811} layer slightly more compact than the pristine layer due to the bi-modal particle size distribution. Shodiev et al. have shown that having a more porous layer close

to the separator and denser layer close to the current collector will have a positive impact on the performance.[33] Hence, the choice of putting the mixed NMC_{811} layer close to the current collector. Structured electrodes have already been reported in the literature either through modeling studies,[33,34] or investigated experimentally through slurry processed electrodes.[35,36] However, the slurry method can lead to inhomogeneous distribution of lighter components (carbon, binder) during the drying step facilitating weak mechanical properties,[37,38] especially for thick electrodes. Moreover, the bi-layer electrode requires 2 different steps of slurry coating and drying, which is not cost/energy efficient. While, for dry coating, stacking two different films and calendaring them together suffices to yield a bi-layer electrode, yet none have been reported in the literature to the authors' knowledge.

To validate the benefit of this design, 1 C discharge simulations comparison was performed between a pristine electrode, and a bi-layer electrode, both sharing the same top layer. The bottom layer of the bilayer electrode consisted of 75 wt.% of pristine particles and 25 wt.% of the same particles but shrunk. Due to the associated computational cost, it was impossible to use primary particles instead of secondary ones for the ball-milled particles to mimic the experiment (see **Figure S2**). The 3-D distribution of the SOD at the end of discharge is represented for the pristine and bi-layer electrodes respectively in **Figure 3A** and **Figure 3B**. Since 3-D visuals can be hard to interpretate, **Figure 3C** offers a quantitative comparison of the average SOD along the thickness of both electrodes. Regarding the top layer, the two electrodes share a similar NMC_{811} utilization, but there is a significant improvement at the bottom layer of the bi-layer design. The bi-layer electrode achieves a discharge capacity 11% superior to the pristine one at 8 mA/cm^2 (1 C), mostly due to a higher utilization of the bottom layer thanks to the new bi-layer architecture. The opposite configuration with the mixed NMC_{811} layer being near the separator has also been investigated.

As confirmed through modeling and experiments in **Figure S3** and **S4**, stronger gradients and a decay in performance are observed, further validating the structured electrode adopted in this work.

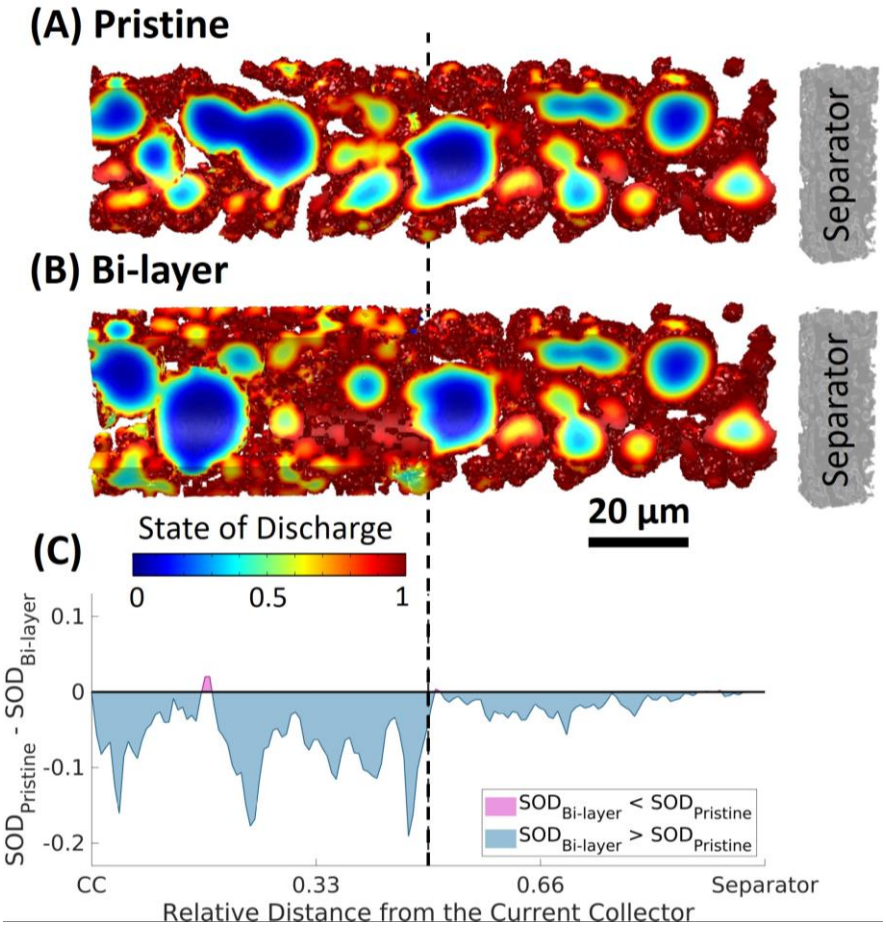

Figure 3. Modeling Validation of the Structured Bi-layer Electrode Design

Simulated 3-D distribution of the state of discharge at the end of a 1 C discharge for the (A) Pristine and (B) Bi-layer cases. Both electrodes share the same right half, only the left half is different. (C) Difference in the average state of discharge as a function of the distance from the current collector between the Pristine (A) and Bi-layer (B).

Experimental Validation for the Bi-Layer Thick Electrode

Based on the insights gathered from the coupling of FEM and ML, a bi-layer structured electrode was proposed to decrease the volume of particles and increase their specific surface area. Further modeling investigations demonstrated the effectiveness of this design to improve the rate capability compared to the pristine electrode. To prove the capability of this modeling workflow, 3 coin cells were fabricated for the pristine and bi-layer electrodes, which were paired with lithium foils as the counter electrode.

Electrodes with a loading of 8 mAh/cm² (ca. 150 µm) were manufactured with the dry process method using NMC_{811} (LG Chem), VGCF (Sigma Aldrich), and PTFE (Chemours) following a weight ratio of 93 : 5 : 2. In the case of the bi-layer, within the 93 wt.% of NMC_{811}, 75 wt.% were pristine and 25 wt.% were ball-milled NMC_{811}. **Figure 4A** shows the morphology of a bi-layer electrode in the case of a bottom layer with twice the amount of ball-milled particles and binder to enable a robust film. The volume of ball-milled particles has been increased to enhance the visual difference between the two layers, but scanning electron microscope images of a pristine and standard bi-layer electrodes are available in **Figure S5**. While we do observe a larger number of pristine NMC_{811} particles at the top and a larger number of primary particles at the bottom, ball-milled particles can still be found even close to the separator, i.e. the pristine layer. This could be induced by the calendaring process, indeed NMC_{811} is known to be prone to cracking, especially the region close to the separator/calendaring roll.[39] Furthermore, some degree of merging of the two layers could be expected at their interface since they are two soft and porous films. Despite the slight deviation from the ideal design investigated in the modeling study, a bi-layer structured electrode was still achieved.

A formation cycle at 0.4 mA/cm² (C/20) was followed by a discharge rate test ranging from 0.8 to 8 mA/cm² (C/10 to 1 C), with a constant charge at 1.6 mA/cm² (C/5). The areal loading was fixed at 8 mAh/cm² (40 mg_{NMC}/cm^2), which is twice the commercial standard currently used. The rate tests results are summarized in **Figure 4B**, and the discharge curves are presented in **Figure 4C**. Similar discharge capacities are obtained at low rate until the C/2 threshold where the bi-layer outperforms the pristine electrode. The bi-layer half-cells achieve an average discharge capacity at a current density of 8 mA/cm² (1 C) of 86 mAh/g_{NMC}, and an average of 168 mAh/g_{NMC} at 4 mA/cm² (C/2), respectively around 125% and 25% higher than the pristine coin cells. The dispersion of values at a given rate is negligeable at low rates (range of ca 7 mAh/g_{NMC} at C/10 for the bi-layer) but significantly increases at higher rates (range of ca. 54 mAh/g_{NMC} at 1C for the bi-layer) as one could have expected. Such variations are inherent to the manual manufacturing of thick electrodes through dry processing.

These performances are particularly impressive when compared to the reported thick NMC electrodes discharge capacities for the same rates. **Figure 5** highlights how this work's results stand out from the literature in terms of discharge capacities for such a high loading. While this study uses a constant charge rate during the discharge rate tests which can boost the capacity compared to a symmetric rate test, it is noteworthy that most of the data points reported in **Figure 5** are obtained by using further electrode modification (laser structuring for instance). Another significant difference is the volumetric capacity achieved by the bi-layer coin cells (ca. 450 Ah/L) which is almost twice as much as the other electrodes. The volumetric capacity is particularly of interest for small nomadic devices (laptop, phones, etc…), where the space allocated to the battery is minimal. Such an impressive volumetric capacity stems from the high discharge capacity at such a high loading, but also from the low porosity achieved by the dry coating method (ca. 30%),

significantly lower than the standard porosity for thick electrodes, usually over 40%. Additionally, thanks to the areal loading (8 mAh/cm²) twice as high as the conventional one, a cell pack with the same capacity would require a lighter weight, owed to less modules required inside a pack. This higher gravimetric capacity is a key factor to the development of batteries for electric vehicles, hence the active research on thick electrodes. The dry processing combined with the bi-layer design presented here is promising because it yields both a high volumetric capacity at the electrode level and a high gravimetric capacity at the pack level at high rates.

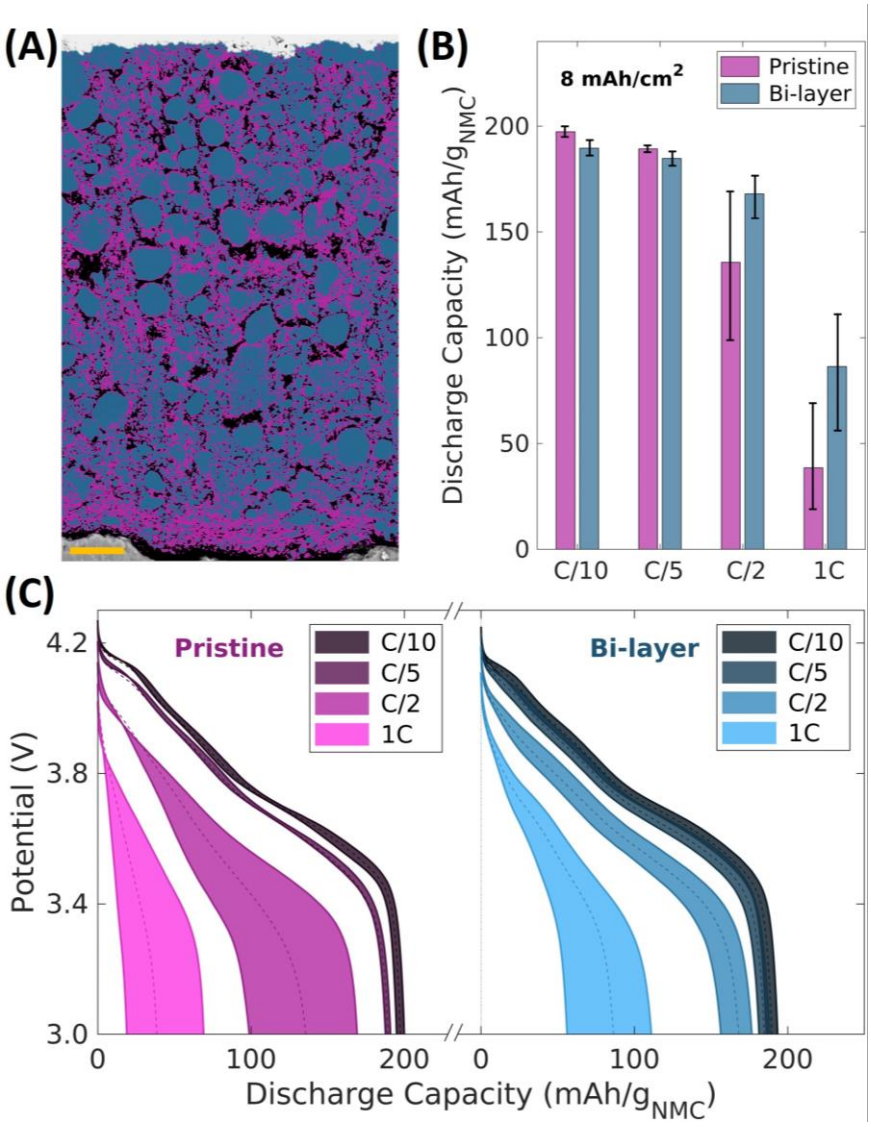

Figure 4. (A) Scanning electron microscope image of a bi-layer electrode with twice the amount of ball-milled NMC_{811} and PTFE in the bottom layer. The NMC_{811} is represented in blue, the VGCF+PTFE in purple, the current collector in gray and the pores in black. The image has been segmented based on the gray levels in MATLAB. The scale bar represents 15 µm (B) Discharge rates comparison between the pristine and bi-layer cases in coin cells with an areal loading close to ca. 8 mAh/cm² and a constant charge at C/5. The bars represent the average value, and the error-bars represents the maximal and minimal values. (C) Discharge curves for the pristine and bi-layer cases at different discharge rates. For each rate, the shaded area are delimited by the discharge curves of the half-cells with the largest and smallest discharge capacities, and the dashed line represents the average discharge curve of all cells.

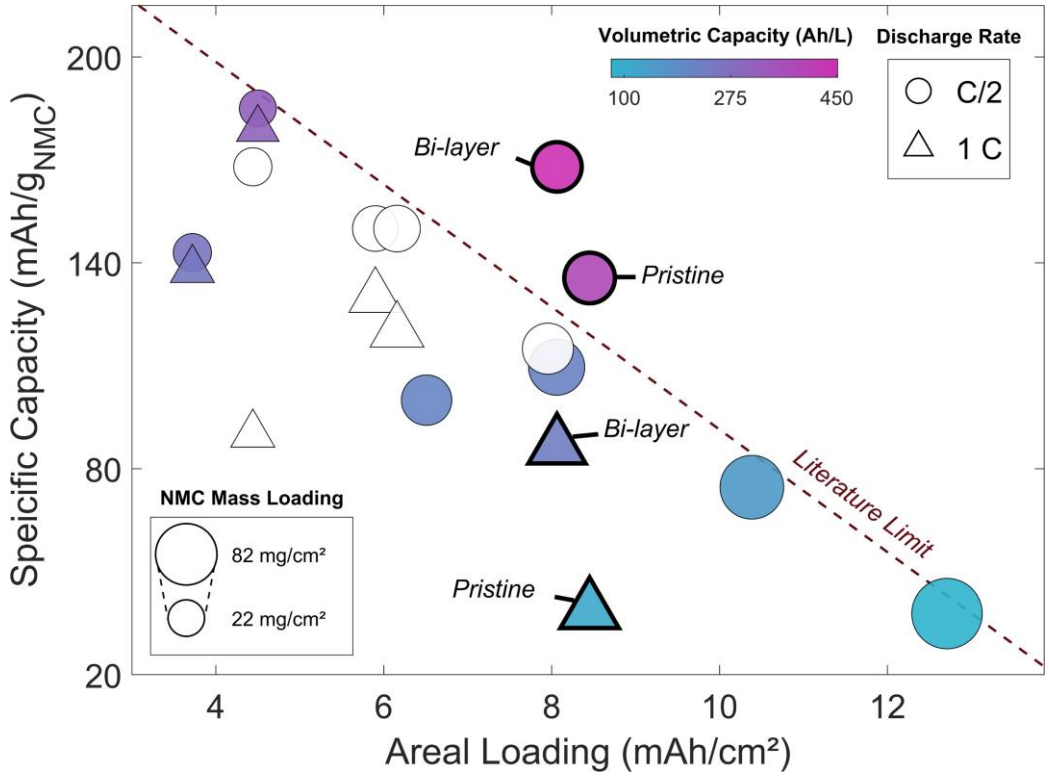

Figure 5. Literature review of the discharge capacity of thick NMC electrodes at high rates as a function of the areal loading and the volumetric capacity.[1,36,40–44] For the bi-layer and pristine cases

presented in this work, the average coin cells results are represented with thicker edges. The size of the symbols is proportional to the NMC mass loading and the color white represents data points for which the volumetric capacity could not be calculated. See Table S3 for the complete summary of the data used in this plot.

In this work an ML model has been trained using a limited number of lengthy FEM simulations and could yield dynamic SOD predictions for thick NMC_{811} electrodes with only 7.3% of relative error. This unique FEM-ML coupling workflow draws its strength from having each particle in the electrode as a data point instead of each FEM simulation, significantly cutting down the required FEM simulations to build a large enough dataset to train an ML model. The latter has a computation time 2 orders of magnitude lower than the FEM, allowing wide screenings of parameters which are too costly with FEM.

Subsequently, more in depth understanding of the limiting phenomena during the discharge have been evidenced using XAI through the study of SHAP values. The ionic transport and the morphology of the NMC_{811} particles were identified as the most impactful parameters during the lithiation of the positive electrode. The methodology of this work is promising and could be applied to a number of different systems to gain insights and address the bottlenecks in the battery fields. To promote the implementation of this approach, all the computational files necessary to reproduce the workflow are provided to the community in the SI.

Based on those insights, a structured bi-layer electrode with a layer close to the current collector consisting of a mix of pristine and ball-milled NMC_{811} was implemented. Its ability to improve the performance at rates as high as 8 mA/cm² were first investigated through modeling and then further verified through experimental validation. The bi-layer electrodes displayed the highest volumetric

capacity (450 Ah/L) than any reported thick NMC electrodes at such C-rates, twice as much as an electrode with a similar loading and discharge rate. The impressive performance with dense thick electrodes and the simplicity of the manufacturing process to obtain bi-layer dry electrodes is promising for its scalability at the industrial level.

ASSOCIATED CONTENT

Supporting Information.

Experimental Section, Figures S1-S5, and Table S1-S3. (PDF)

All the MATLAB/Python codes and COMSOL template will be made available upon publication.

AUTHOR INFORMATION

Further information and requests for resources should be directed to and will be fulfilled by the Lead Contact, Ying S. Meng (shirleymeng@uchicago.edu).

Notes

The authors declare no competing financial interest.

ACKNOWLEDGMENT

The authors are grateful to LG Chem for providing the NMC_{811} powder and to Chemours for providing the PTFE powder used in this study. The authors acknowledge C. Hamill at the University of Chicago for the server network administration. The FIB-SEM in this work were performed in part at the San Diego Nanotechnology Infrastructure (SDNI) of UCSD, a member of the National Nanotechnology Coordinated Infrastructure, which is supported by the National Science Foundation (Grant ECCS-1542148). The authors thank the University of Chicago - France program (FACCTS, 2023) for its financial support.

REFERENCES

(1) Zheng, H.; Li, J.; Song, X.; Liu, G.; Battaglia, V. S. A Comprehensive Understanding of Electrode Thickness Effects on the Electrochemical Performances of Li-Ion Battery Cathodes. *Electrochimica Acta* **2012**, *71*, 258–265. https://doi.org/10.1016/j.electacta.2012.03.161.

(2) Zhang, X.; Ju, Z.; Zhu, Y.; Takeuchi, K. J.; Takeuchi, E. S.; Marschilok, A. C.; Yu, G. Multiscale Understanding and Architecture Design of High Energy/Power Lithium-Ion Battery Electrodes. *Advanced Energy Materials* **2021**, *11* (2), 2000808. https://doi.org/10.1002/aenm.202000808.

(3) Chiu, R. C.; Garino, T. J.; Cima, M. J. Drying of Granular Ceramic Films: I, Effect of Processing Variables on Cracking Behavior. *Journal of the American Ceramic Society* **1993**, *76* (9), 2257–2264. https://doi.org/10.1111/j.1151-2916.1993.tb07762.x.

(4) Singh, K. B.; Tirumkudulu, M. S. Cracking in Drying Colloidal Films. *Phys. Rev. Lett.* **2007**, *98* (21), 218302. https://doi.org/10.1103/PhysRevLett.98.218302.

(5) Zhang, X.; Zhu, Y.; Bruck, A. M.; Housel, L. M.; Wang, L.; Quilty, C. D.; Takeuchi, K. J.; Takeuchi, E. S.; Marschilok, A. C.; Yu, G. Understanding Aggregation Hindered Li-Ion Transport in Transition Metal Oxide at Mesoscale. *Energy Storage Materials* **2019**, *19*, 439–445. https://doi.org/10.1016/j.ensm.2019.03.017.

(6) Kuang, Y.; Chen, C.; Kirsch, D.; Hu, L. Thick Electrode Batteries: Principles, Opportunities, and Challenges. *Advanced Energy Materials* **2019**, *9* (33), 1901457. https://doi.org/10.1002/aenm.201901457.

(7) Chouchane, M.; Franco, A. A. Deconvoluting the Impacts of the Active Material Skeleton and the Inactive Phase Morphology on the Performance of Lithium Ion Battery Electrodes. *Energy Storage Materials* **2022**, *47*, 649–655. https://doi.org/10.1016/j.ensm.2022.02.016.

(8) Danner, T.; Singh, M.; Hein, S.; Kaiser, J.; Hahn, H.; Latz, A. Thick Electrodes for Li-Ion Batteries: A Model Based Analysis. *Journal of Power Sources* **2016**, *334*, 191–201. https://doi.org/10.1016/j.jpowsour.2016.09.143.

(9) Lu, X.; Bertei, A.; Finegan, D. P.; Tan, C.; Daemi, S. R.; Weaving, J. S.; O'Regan, K. B.; Heenan, T. M. M.; Hinds, G.; Kendrick, E.; Brett, D. J. L.; Shearing, P. R. 3D Microstructure Design of Lithium-Ion Battery Electrodes Assisted by X-Ray Nano-Computed Tomography and Modelling. *Nat Commun* **2020**, *11* (1), 2079. https://doi.org/10.1038/s41467-020-15811-x.

(10) Severson, K. A.; Attia, P. M.; Jin, N.; Perkins, N.; Jiang, B.; Yang, Z.; Chen, M. H.; Aykol, M.; Herring, P. K.; Fraggedakis, D.; Bazant, M. Z.; Harris, S. J.; Chueh, W. C.; Braatz, R. D. Data-Driven Prediction of Battery Cycle Life before Capacity Degradation. *Nat Energy* **2019**, *4* (5), 383–391. https://doi.org/10.1038/s41560-019-0356-8.

(11) Marcato, A.; Santos, J. E.; Liu, C.; Boccardo, G.; Marchisio, D.; Franco, A. A. Modeling the 4D Discharge of Lithium-Ion Batteries with a Multiscale Time-Dependent Deep Learning Framework. *Energy Storage Materials* **2023**, 102927. https://doi.org/10.1016/j.ensm.2023.102927.

(12) Goel, V.; Chen, K.-H.; Dasgupta, N. P.; Thornton, K. Optimization of Laser-Patterned Electrode Architectures for Fast Charging of Li-Ion Batteries Using Simulations Parameterized by Machine Learning. *Energy Storage Materials* **2023**, *57*, 44–58. https://doi.org/10.1016/j.ensm.2023.01.050.

(13) Gao, T.; Lu, W. Physical Model and Machine Learning Enabled Electrolyte Channel Design for Fast Charging. *J. Electrochem. Soc.* **2020**, *167* (11), 110519. https://doi.org/10.1149/1945-7111/aba096.
(14) Drakopoulos, S. X.; Gholamipour-Shirazi, A.; MacDonald, P.; Parini, R. C.; Reynolds, C. D.; Burnett, D. L.; Pye, B.; O'Regan, K. B.; Wang, G.; Whitehead, T. M.; Conduit, G. J.; Cazacu, A.; Kendrick, E. Formulation and Manufacturing Optimization of Lithium-Ion Graphite-Based Electrodes via Machine Learning. *Cell Reports Physical Science* **2021**, *2* (12), 100683. https://doi.org/10.1016/j.xcrp.2021.100683.
(15) Lundberg, S. M.; Lee, S.-I. A Unified Approach to Interpreting Model Predictions. In *Advances in Neural Information Processing Systems*; Curran Associates, Inc., 2017; Vol. 30.
(16) Yao, W.; Chouchane, M.; Li, W.; Bai, S.; Liu, Z.; Li, L.; Chen, A. X.; Sayahpour, B.; Shimizu, R.; Raghavendran, G.; Schroeder, M. A.; Chen, Y.-T.; Tan, D. H. S.; Sreenarayanan, B.; Waters, C. K.; Sichler, A.; Gould, B.; Kountz, D. J.; Lipomi, D. J.; Zhang, M.; Meng, Y. S. A 5 V-Class Cobalt-Free Battery Cathode with High Loading Enabled by Dry Coating. *Energy Environ. Sci.* **2023**, *16* (4), 1620–1630. https://doi.org/10.1039/D2EE03840D.
(17) Chouchane, M.; Franco, A. A. About the Consideration of the Inactive Materials and the Meshing Procedures in Computational Models of Lithium Ion Battery Electrodes. *ChemElectroChem* **2022**, *9* (21), e202200692. https://doi.org/10.1002/celc.202200692.
(18) Zhang, M.; Chouchane, M.; Shojaee, S. A.; Winiarski, B.; Liu, Z.; Li, L.; Pelapur, R.; Shodiev, A.; Yao, W.; Doux, J.-M.; Wang, S.; Li, Y.; Liu, C.; Lemmens, H.; Franco, A. A.; Meng, Y. S. Coupling of Multiscale Imaging Analysis and Computational Modeling for Understanding Thick Cathode Degradation Mechanisms. *Joule* **2023**, *7* (1), 201–220. https://doi.org/10.1016/j.joule.2022.12.001.
(19) Tran, A. P.; Yan, S.; Fang, Q. Improving Model-Based Functional near-Infrared Spectroscopy Analysis Using Mesh-Based Anatomical and Light-Transport Models. *NPh* **2020**, *7* (1), 015008. https://doi.org/10.1117/1.NPh.7.1.015008.
(20) Chouchane, M.; Rucci, A.; Lombardo, T.; Ngandjong, A. C.; Franco, A. A. Lithium Ion Battery Electrodes Predicted from Manufacturing Simulations: Assessing the Impact of the Carbon-Binder Spatial Location on the Electrochemical Performance. *Journal of Power Sources* **2019**, *444*, 227285. https://doi.org/10.1016/j.jpowsour.2019.227285.
(21) Lu, X.; Daemi, S. R.; Bertei, A.; Kok, M. D. R.; O'Regan, K. B.; Rasha, L.; Park, J.; Hinds, G.; Kendrick, E.; Brett, D. J. L.; Shearing, P. R. Microstructural Evolution of Battery Electrodes During Calendering. *Joule* **2020**, *4* (12), 2746–2768. https://doi.org/10.1016/j.joule.2020.10.010.
(22) COMSOL Multiphysics Reference Manual.
(23) Cooper, S. J.; Bertei, A.; Shearing, P. R.; Kilner, J. A.; Brandon, N. P. TauFactor: An Open-Source Application for Calculating Tortuosity Factors from Tomographic Data. *SoftwareX* **2016**, *5*, 203–210. https://doi.org/10.1016/j.softx.2016.09.002.
(24) Gilpin, L. H.; Bau, D.; Yuan, B. Z.; Bajwa, A.; Specter, M.; Kagal, L. Explaining Explanations: An Overview of Interpretability of Machine Learning. In *2018 IEEE 5th International Conference on Data Science and Advanced Analytics (DSAA)*; IEEE: Turin, Italy, 2018; pp 80–89. https://doi.org/10.1109/DSAA.2018.00018.
(25) Nair, P.; Vakharia, V.; Borade, H.; Shah, M.; Wankhede, V. Predicting Li-Ion Battery Remaining Useful Life: An XDFM-Driven Approach with Explainable AI. *Energies* **2023**, *16* (15), 5725. https://doi.org/10.3390/en16155725.

(26) Lee, G.; Kim, J.; Lee, C. State-of-Health Estimation of Li-Ion Batteries in the Early Phases of Qualification Tests: An Interpretable Machine Learning Approach. *Expert Systems with Applications* **2022**, *197*, 116817. https://doi.org/10.1016/j.eswa.2022.116817.
(27) Lundberg, S. M.; Erion, G.; Chen, H.; DeGrave, A.; Prutkin, J. M.; Nair, B.; Katz, R.; Himmelfarb, J.; Bansal, N.; Lee, S.-I. From Local Explanations to Global Understanding with Explainable AI for Trees. *Nat Mach Intell* **2020**, *2* (1), 56–67. https://doi.org/10.1038/s42256-019-0138-9.
(28) Lundberg, S. M.; Erion, G. G.; Lee, S.-I. Consistent Individualized Feature Attribution for Tree Ensembles. arXiv March 6, 2019. http://arxiv.org/abs/1802.03888 (accessed 2023-10-23).
(29) Zhang, J.; Qiao, J.; Sun, K.; Wang, Z. Balancing Particle Properties for Practical Lithium-Ion Batteries. *Particuology* **2022**, *61*, 18–29. https://doi.org/10.1016/j.partic.2021.05.006.
(30) Pfleging, W. A Review of Laser Electrode Processing for Development and Manufacturing of Lithium-Ion Batteries. *Nanophotonics* **2018**, *7* (3), 549–573. https://doi.org/10.1515/nanoph-2017-0044.
(31) Hille, L.; Noecker, M. P.; Ko, B.; Kriegler, J.; Keilhofer, J.; Stock, S.; Zaeh, M. F. Integration of Laser Structuring into the Electrode Manufacturing Process Chain for Lithium-Ion Batteries. *Journal of Power Sources* **2023**, *556*, 232478. https://doi.org/10.1016/j.jpowsour.2022.232478.
(32) Pfleging, W. Recent Progress in Laser Texturing of Battery Materials: A Review of Tuning Electrochemical Performances, Related Material Development, and Prospects for Large-Scale Manufacturing. *Int. J. Extrem. Manuf.* **2020**, *3* (1), 012002. https://doi.org/10.1088/2631-7990/abca84.
(33) Shodiev, A.; Chouchane, M.; Gaberscek, M.; Arcelus, O.; Xu, J.; Oularbi, H.; Yu, J.; Li, J.; Morcrette, M.; Franco, A. A. Deconvoluting the Benefits of Porosity Distribution in Layered Electrodes on the Electrochemical Performance of Li-Ion Batteries. *Energy Storage Materials* **2022**, *47*, 462–471. https://doi.org/10.1016/j.ensm.2022.01.058.
(34) Lu, X.; Zhang, X.; Tan, C.; M. Heenan, T. M.; Lagnoni, M.; O'Regan, K.; Daemi, S.; Bertei, A.; G. Jones, H.; Hinds, G.; Park, J.; Kendrick, E.; L. Brett, D. J.; R. Shearing, P. Multi-Length Scale Microstructural Design of Lithium-Ion Battery Electrodes for Improved Discharge Rate Performance. *Energy & Environmental Science* **2021**, *14* (11), 5929–5946. https://doi.org/10.1039/D1EE01388B.
(35) Chowdhury, R.; Zhao, Y.; Xia, Y.; Ouyang, M.; Brandon, N.; Banerjee, A. Revisiting the Promise of Bi-Layer Graded Cathodes for Improved Li-Ion Battery Performance. *Sustainable Energy & Fuels* **2021**, *5* (20), 5193–5204. https://doi.org/10.1039/D1SE01077H.
(36) Song, Z.; Zhu, P.; Pfleging, W.; Sun, J. Electrochemical Performance of Thick-Film Li(Ni0.6Mn0.2Co0.2)O2 Cathode with Hierarchic Structures and Laser Ablation. *Nanomaterials* **2021**, *11* (11), 2962. https://doi.org/10.3390/nano11112962.
(37) Klemens, J.; Schneider, L.; Herbst, E. C.; Bohn, N.; Müller, M.; Bauer, W.; Scharfer, P.; Schabel, W. Drying of NCM Cathode Electrodes with Porous, Nanostructured Particles Versus Compact Solid Particles: Comparative Study of Binder Migration as a Function of Drying Conditions. *Energy Technology* **2022**, *10* (4), 2100985. https://doi.org/10.1002/ente.202100985.
(38) Font, F.; Protas, B.; Richardson, G.; Foster, J. M. Binder Migration during Drying of Lithium-Ion Battery Electrodes: Modelling and Comparison to Experiment. *Journal of Power Sources* **2018**, *393*, 177–185. https://doi.org/10.1016/j.jpowsour.2018.04.097.

(39) Heenan, T. M. M.; Wade, A.; Tan, C.; Parker, J. E.; Matras, D.; Leach, A. S.; Robinson, J. B.; Llewellyn, A.; Dimitrijevic, A.; Jervis, R.; Quinn, P. D.; Brett, D. J. L.; Shearing, P. R. Identifying the Origins of Microstructural Defects Such as Cracking within Ni-Rich NMC811 Cathode Particles for Lithium-Ion Batteries. *Advanced Energy Materials* **2020**, *10* (47), 2002655. https://doi.org/10.1002/aenm.202002655.
(40) Singh, M.; Kaiser, J.; Hahn, H. A Systematic Study of Thick Electrodes for High Energy Lithium Ion Batteries. *Journal of Electroanalytical Chemistry* **2016**, *782*, 245–249. https://doi.org/10.1016/j.jelechem.2016.10.040.
(41) Singh, M.; Kaiser, J.; Hahn, H. Effect of Porosity on the Thick Electrodes for High Energy Density Lithium Ion Batteries for Stationary Applications. *Batteries* **2016**, *2* (4), 35. https://doi.org/10.3390/batteries2040035.
(42) Du, Z.; Rollag, K. M.; Li, J.; An, S. J.; Wood, M.; Sheng, Y.; Mukherjee, P. P.; Daniel, C.; Wood, D. L. Enabling Aqueous Processing for Crack-Free Thick Electrodes. *Journal of Power Sources* **2017**, *354*, 200–206. https://doi.org/10.1016/j.jpowsour.2017.04.030.
(43) Hu, J.; Wu, B.; Cao, X.; Bi, Y.; Chae, S.; Niu, C.; Xiao, B.; Tao, J.; Zhang, J.; Xiao, J. Evolution of the Rate-Limiting Step: From Thin Film to Thick Ni-Rich Cathodes. *Journal of Power Sources* **2020**, *454*, 227966. https://doi.org/10.1016/j.jpowsour.2020.227966.
(44) Park, S.-H.; King, P. J.; Tian, R.; Boland, C. S.; Coelho, J.; Zhang, C. (John); McBean, P.; McEvoy, N.; Kremer, M. P.; Daly, D.; Coleman, J. N.; Nicolosi, V. High Areal Capacity Battery Electrodes Enabled by Segregated Nanotube Networks. *Nat Energy* **2019**, *4* (7), 560–567. https://doi.org/10.1038/s41560-019-0398-y.

Overview of *ACS Energy Letters* Manuscript Format